SCIENCE CHINA
Technological Sciences

• RESEARCH PAPER •

December 2025, Vol. 68, Iss. 12, 2220301:1–2220301:10
https://doi.org/10.1007/s11431-025-3109-3

Fabric-based cellular pneumatic actuators with programmable shape morphing and high stiffness variation for soft wearable robots

Dezhi YANG[1,2], Jianing SUN[1,2], Miao FENG[1,2,3], Yexun WEI[1,2], Ningbin ZHANG[1,2], Jieji REN[1,2], Jinhao LI[1,2] & Guoying GU[1,2*]

[1] *State Key Laboratory of Mechanical System and Vibration, School of Mechanical Engineering, Shanghai Jiao Tong University, Shanghai 200240, China*

[2] *Shanghai Key Laboratory of Intelligent Robotics, Shanghai Jiao Tong University, Shanghai 200240, China*

[3] *Southwest Technology and Engineering Research Institute, Chongqing 400039, China*

Received July 2, 2025; accepted October 23, 2025; published online November 20, 2025

Abstract Soft actuators with programmable shape morphing and high stiffness variation are highly demanded in soft wearable applications. However, existing methods often struggle to achieve both capabilities simultaneously. Inspired by bulliform cells, we present a class of fabric-based cellular pneumatic actuators (FCPAs), capable of simultaneous shape morphing and stiffness variation (over 420-fold). The FCPA comprises a fabric shell embedded with fabric air chambers: the fabric shell provides geometric constraints to determine target shapes, while the air chambers function as discrete stiffness-tuning elements. A theoretical model is developed to guide the analysis and design of FCPAs, with model predictions agreeing well with experimental results. As a result, we can design and fabricate FCPAs with programmable shapes (such as "S", "W", and "R" shapes) and high load capability (> 5 kg). By customizing the FCPAs, we further develop a soft wearable robot for shoulder abduction assistance and validate its effectiveness on a mannequin and a human subject. These results showcase the unique features of our FCPAs and their huge potential in soft wearable applications.

Keywords soft pneumatic actuator, wearable robot, soft robot application, shape morphing, variable stiffness

Citation: Yang D Z, Sun J N, Feng M, et al. Fabric-based cellular pneumatic actuators with programmable shape morphing and high stiffness variation for soft wearable robots. Sci China Tech Sci, 2025, 68(12): 2220301, https://doi.org/10.1007/s11431-025-3109-3

1 Introduction

Soft wearable robots (SWRs) present an emerging assistive technology designed to support manual workers and rehabilitate patients with mobility impairments [1–5]. Powered by soft actuators, SWRs offer significant advantages over rigid exoskeletons, including safer human-robot interaction, lighter weight, and lower cost [6–8]. To ensure effective assistance and comfortable wearability, SWRs are expected to (1) provide sufficient forces in activated/rigid state, (2) maintain mechanical transparency in deactivated/flexible state, and (3) conform to human body profiles to distribute interaction forces. One key challenge in meeting these requirements is designing soft actuators with programmable shape morphing and high stiffness variation.

Programmable shape morphing has been extensively explored in stimuli-responsive materials and pneumatic soft actuators, leveraging their biomimetic deformations and high scalability. In stimuli-responsive systems, smart materials such as liquid crystal elastomers, shape memory polymers, and hydrogels are typically fabricated into patterned bilayer or multilayer architectures to achieve out-of-plane deformations [9–11]. Pneumatic soft actuators, on the other hand, employ strategies that include designing the arrangement of strain-limiting components (e.g., fibers and patches) [12–14], programming the routes or orientations of air

* Corresponding author (email: guguoying@sjtu.edu.cn)

chambers [15,16], and gradually changing the wall thickness [17,18]. However, since these soft actuators primarily consist of soft, stretchable materials, they exhibit low structural stiffness at target shapes, which limits their applications in high-load-bearing scenarios.

In tackling these challenges, various variable-stiffness methods have been proposed, such as vacuum jamming (granula, fiber, and layer-based) [19,20], mechanical interlocking [21,22], antagonistic actuation [23,24], and the use of low-melting-point alloys [25,26]. Generally, variable-stiffness mechanisms are integrated with soft actuators (embedded or parallel) and change overall structural stiffness once soft actuators morph into desired shapes. While such integrations enable separate control of shape morphing and stiffness variation, they also result in bulky configurations and require complicated control systems. Moreover, variable-stiffness mechanisms may impede the motions of soft actuators.

To achieve simultaneous shape morphing and stiffness variation, one promising strategy is to design and fabricate inflatables with flexible yet minimally stretchable materials [27–31], such as thermoplastic polyurethane (TPU)-coated fabrics. Recent programmable design methods include shaping the pneumatic channels of inflatable fabric beams with hydrosoluble molding [32] and transforming the straightening of simple fabric chambers into desired deformations with X-crossing or lattice structures [33,34]. Another strategy is to assemble rigid or semi-rigid discrete elements under vacuum pressure or tensioned wires [35–37]. Such designs have also demonstrated effectiveness in robotic assistive interfaces [37]. Despite these cumulative advances, designing fully soft actuators that exhibit high performance in shape morphing, stiffness variation, and load capacity remains a significant challenge.

In this work, we present a class of fabric-based cellular pneumatic actuators (FCPAs) capable of simultaneous shape morphing and stiffness variation, and demonstrate their applications in SWRs. Inspired by bulliform cells (Figure 1(a)), which regulate reversible leaf rolling by changing their volume through turgor pressure [38,39], we design the FCPA by embedding fabric air chambers into a fabric shell with multiple through-holes (Figure 1(b)). The through-holes mimic the four-walled architecture of bulliform cells (in cross-section view), while the air chambers replicate the turgor-driven volume change. When the air chambers are pressurized, the FCPA morphs and stiffens, similar to leaf unrolling. We establish a model for analyzing the performance of individual units and the kinematics of FCPAs, with theoretical results consistent with experiments. Guided by the model, we can design and fabricate FCPAs with programmable shapes, such as “S”, “W”, and “R” shapes. Mechanical characterizations (three-point bending and tensile tests) reveal that the “1” shaped and “S” shaped FCPAs can achieve more than 420-fold stiffness tuning and 5 kg load capacity. These properties endow FCPAs with great potential in soft wearable applications, such as a soft exosuit that conforms to the human body profiles and assists in lifting the arm effectively (Figure 1(c)).

The remainder of the paper is organized as follows. Section 2 illustrates the design, working principle, and fabrication process of FCPAs. Section 3 describes the modeling of FCPAs, focusing on the unit bending deformation, unit bending stiffness, and kinematics of multiple units. Section 4 first reveals the influences of parameters on the performance of units, combining theoretical and experimental results. Then, various FCPAs and an exemplary application for shoulder assistance are developed. Section 5 concludes this work.

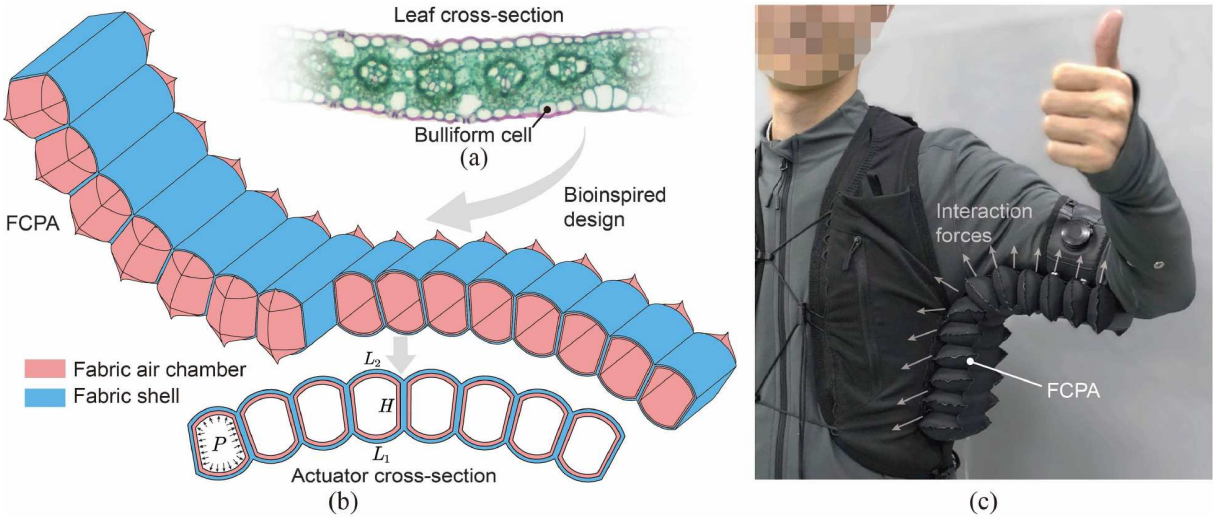

Figure 1 (Color online) Bioinspired design and application of the fabric-based cellular pneumatic actuators (FCPAs). (a) A cross-section of monocotyledonous leaves shows the structure of bulliform cells; (b) structure and working principle of the FCPA; (c) application of the FCPA in a soft wearable robot for shoulder abduction assistance.

2 Design and fabrication

2.1 Design and working principle

The FCPA comprises a fabric shell with multiple through-holes and several embedded fabric air chambers (Figure 2(a)). All the components are constructed from highly flexible yet minimally stretchable woven fabrics (Figure 2(b) and (c)). The fabric shell defines the target shapes through geometric constraints, while the air chambers modulate structural stiffness by adjusting their internal pressure. When deflated, the FCPA is ultra-flexible and foldable, due to its all-fabric construction. When inflated, it morphs into desired shapes with enhanced structural stiffness (Figure 2(d)).

To illustrate the working principle of FCPA, we consider a unit composed of a fabric shell segment with one through-hole and an embedded air chamber. The fabric shell segment features a four-walled structure, with lateral walls of height H and bottom and top walls of lengths L_1 and L_2, respectively (Figure 2(a)). Upon inflation, the air chamber expands and stiffens, supporting the four-walled fabric shell segment. As shown in the actuator cross-section in Figure 1(b), the bottom and top walls tend to bulge into circular arcs to maximize internal volume, while the lateral walls tend to straighten due to the constraints imposed by adjacent units. When L_1 and L_2 are of different lengths, the unit undergoes bending deformation. Consequently, the overall shape morphing of the FCPA can be programmed by tuning the geometric parameters (H, L_1, and L_2) of individual units, as will be modeled in the next section.

To ensure that the air chambers fully support the fabric shell, the flat width of each chamber, W_c (Figure 2(c)), is designed as $W_c = (2H + L_1 + L_2 + 5\ \text{mm})/2$. For fabrication convenience, we keep the sum of L_1 and L_2 as a constant $2L$ (i.e., $L_1 + L_2 = 2L$) and the H as another constant, so that all air chambers within one FCPA share identical dimensions. Moreover, the width of FCPA, W (Figure 2(a)), is set as 80 mm in this work.

2.2 Fabrication

Fabric materials with high elastic moduli and thin thickness are ideal for fabricating the FCPAs. In this work, we empirically choose the TPU-coated 70D Nylon woven fabric (0.22 mm, Jiaxing Yingcheng Textile Co., Ltd.). The elastic modulus of this fabric is approximately 88 MPa (weft) and 185 MPa (wrap). The fabrication process of an FCPA includes the following steps.

(1) Material preparation: The TPU-coated 70D Nylon woven fabric is laser-cut into patterned sheets ①–⑥, and the non-stick baking paper (0.05 mm, Foshan Nanhai Weiji Kitchen Utensil Co., Ltd.) is laser-cut into patterned sheets ⑦ (Figure 2(b) and (c)).

(2) Fabric shell fabrication: First, we heat-press (200°C, 5 s) each pair of fabric sheets ① and ② using a handheld acrylic bending machine (Type A, Jinan Hongyang CNC Machinery Co., Ltd.) to form an I-shaped rib. This process is repeated as needed to fabricate multiple ribs. Then, we heat-press the lower ends of these ribs to the fabric sheet ④.

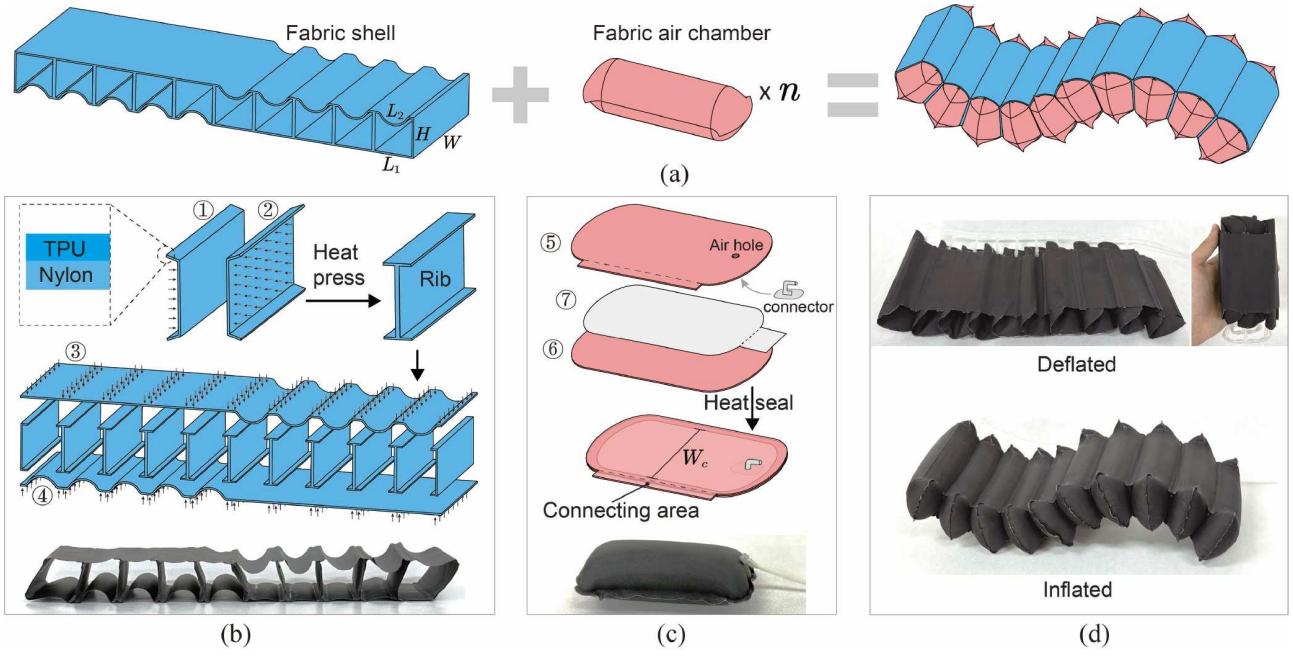

Figure 2 (Color online) Detailed structure and fabrication of the FCPAs. (a) The FCPA consists of a fabric shell with multiple through-holes and several fabric air chambers. The fabric shell determines the programmable shape morphing, while the fabric air chambers are inserted into the shell to tune its stiffness. (b) Fabrication process of the fabric shell; (c) fabrication process of the fabric air chambers; (d) the completed FCPAs are ultra-flexible when deflated, while transforming into target shapes with high stiffness when inflated.

Finally, we heat-press the upper ends of these ribs to the fabric sheet ③, forming a fabric shell with multiple through-holes (Figure 2(b)).

(3) Air chamber fabrication: For each air chamber, first, we align fabric sheet ⑤, baking paper ⑦, and fabric sheet ⑥ in turn and heat-seal (180°C, 30 s) the margin with a heat-press machine (38 cm×38 cm, Yiwu Hexin Digital Technology Co., Ltd.). Then, we assemble the air connector from the inside with glue and cut off the extra baking paper. Finally, we heat-seal (200°C, 5 s) the remaining margin near the air hole with a handheld acrylic bending machine to complete an air chamber. This process is repeated as needed to fabricate multiple air chambers (Figure 2(c)).

(4) Final assembly: For each through-hole on the fabric shell, we insert an air chamber and bond the chamber's connecting area to the top wall via heat-pressing. This ensures secure embedding of the air chamber within the fabric shell, preventing relative displacement. We repeat this process in turn to complete the assembly.

3 Modeling

In this section, we present a theoretical model that predicts the performance of individual units and the kinematics of multiple units, guiding the design of FCPAs in terms of shape morphing and structural stiffness. The following assumptions are made: (1) the fabric material is non-stretchable and has negligible thickness and flexural rigidity; (2) the cross-section of FCPA is uniform across its width; (3) for all units, the lateral walls are straight while the bottom and top walls bulge into circular arcs upon inflation (Figure 3(a)).

3.1 Force balance equation system

Considering the geometric symmetry, we perform a force analysis on half of the unit (Figure 3(b)). Three external forces act on the half-unit: the actuation pressure P, the tension on the bottom wall T_1, and the tension on the top wall T_2. The horizontal and vertical force balance yields

$$T_2+T_1=P\left[H\cos\frac{\alpha_0}{2}+R_2\left(1-\cos\frac{\theta_2}{2}\right)+R_1\left(1-\cos\frac{\theta_1}{2}\right)\right], \quad (1)$$

$$PR_2\sin\frac{\theta_2}{2}=P\left(H\sin\frac{\alpha_0}{2}+R_1\sin\frac{\theta_1}{2}\right), \quad (2)$$

where R_1, R_2, θ_1, θ_2, and α_0 represent the radius of the bottom wall, radius of the top wall, central angle of the bottom wall, central angle of the top wall, and force-free bending angle of the unit, respectively. By balancing the torque resulting from T_1, T_2, and P with respect to the midpoint of the axis of symmetry C1-C2, we can obtain

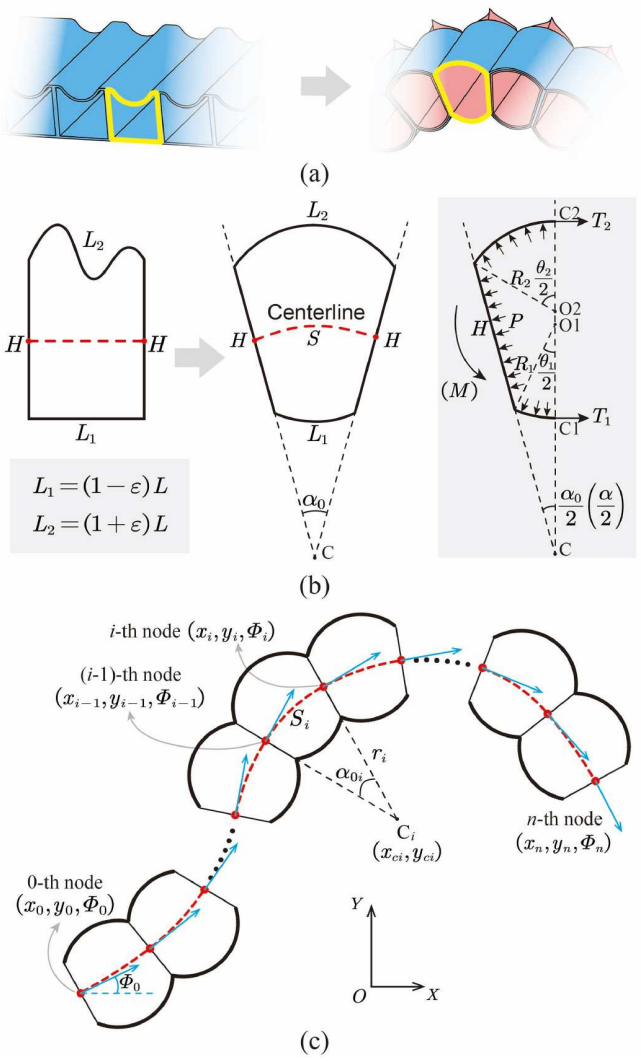

Figure 3 (Color online) Modeling of the FCPAs. (a) The evolution of the cross-sectional geometry of FCPAs before and after inflation. The yellow line indicates one unit of the FCPAs. (b) Deformation and force analysis of the unit; (c) the kinematics of multiple units. The centerlines are calculated to predict the shape morphing of FCPAs.

$$\frac{W(T_2-T_1)}{2}\left[H\cos\frac{\alpha_0}{2}+R_2\left(1-\cos\frac{\theta_2}{2}\right)+R_1\left(1-\cos\frac{\theta_1}{2}\right)\right]=0. \quad (3)$$

Since the actuation pressure P can be also regarded as acting along the C1-C2 axis, it generates no net torque.

Eqs. (1)–(3) constitute the force balance equation system. The intermediate variables (T_1, T_2, R_1, R_2, θ_1, and θ_2) are mutually coupled. Following Laplace's law for membranes, the induced tensions (T_1 and T_2) and curvatures (R_1 and R_2) are related to the actuation pressure P as

$$P=\frac{T_1}{R_1}=\frac{T_2}{R_2}. \quad (4)$$

Since the fabric is non-stretchable, the wall radii (R_1 and

R_2) and the central angles (θ_1 and θ_2) are related to the wall lengths (L_1 and L_2) as

$$R_1\theta_1 = L_1, \quad R_2\theta_2 = L_2. \tag{5}$$

3.2 Unit bending deformation

We describe the bending deformation of the unit with two parameters: α_0 and the centerline length S, which can be solved from the force balance equation system. Combining eqs. (3) and (4), we find that the tensions and radii of the bottom and top walls are identical:

$$T_1 = T_2, \quad R_1 = R_2. \tag{6}$$

Substituting eq. (4) into eq. (1) and simplifying eq. (2), we get

$$\begin{cases} H\cos\dfrac{\alpha_0}{2} = R_2\cos\dfrac{\theta_2}{2} + R_1\cos\dfrac{\theta_1}{2}, \\ H\sin\dfrac{\alpha_0}{2} = R_2\sin\dfrac{\theta_2}{2} - R_1\sin\dfrac{\theta_1}{2}, \end{cases} \tag{7}$$

which reveals that the arc centers of the bottom and top walls (O1 and O2) coincide. Combining eqs. (5)–(7), α_0 can be solved as

$$\alpha_0 = \begin{cases} \dfrac{L_2 - L_1}{H}\cos\left(\dfrac{\alpha_0}{2}\dfrac{L_2 + L_1}{L_2 - L_1}\right), & L_1 \neq L_2, \\ 0, & L_1 = L_2. \end{cases} \tag{8}$$

To normalize the length, we introduce an asymmetry degree ε to describe the difference between L_1 and L_2,

$$\begin{cases} L_1 = (1-\varepsilon)L, \\ L_2 = (1+\varepsilon)L, \end{cases} \tag{9}$$

where $-1 < \varepsilon < 1$. Substituting eq. (9) into eq. (8), eq. (8) can be written as

$$\alpha_0 = \begin{cases} 2\varepsilon\left(\dfrac{L}{H}\right)\cos\left(\dfrac{\alpha_0}{2\varepsilon}\right), & -1 < \varepsilon < 1 \ \& \ \varepsilon \neq 0, \\ 0, & \varepsilon = 0. \end{cases} \tag{10}$$

As the unit undergoes bending deformation, we define the centerline as the arc centered at C, spanning between the midpoints of the lateral walls (Figure 3(b)). Because O1 and O2 coincide and $R_1 = R_2$, S can be calculated as

$$S = \frac{R_1\sin\left(\dfrac{\theta_1}{2} + \dfrac{\alpha_0}{2}\right)}{\tan\left(\dfrac{\alpha_0}{2}\right)}\alpha_0 = \varepsilon L\frac{\sin\left(\dfrac{\alpha_0}{2\varepsilon}\right)}{\tan\left(\dfrac{\alpha_0}{2}\right)}, \alpha_0 \neq 0. \tag{11}$$

In the special case where $\alpha_0 = 0$ (i.e., the lateral walls are vertical), the previous expression becomes undefined. In this case, S is instead given by

$$S = 2R_1\sin\left(\frac{L}{2R_1}\right), \tag{12}$$

where R_1 satisfies $\dfrac{H}{2R_1} = \cos\left(\dfrac{L}{2R_1}\right)$.

3.3 Unit bending stiffness

To evaluate the bending stiffness, we consider the application of an external torque M to the unit, which causes the bending angle to vary from α_0 to α (Figure 3(b)). The force balance eqs. (1) and (2) remain valid and can be reduced to a form involving two intermediate variables:

$$\begin{cases} H\cos\dfrac{\alpha}{2} = \dfrac{(1+\varepsilon)L}{\theta_2}\cos\dfrac{\theta_2}{2} + \dfrac{(1-\varepsilon)L}{\theta_1}\cos\dfrac{\theta_1}{2}, \\ H\sin\dfrac{\alpha}{2} = \dfrac{(1+\varepsilon)L}{\theta_2}\sin\dfrac{\theta_2}{2} - \dfrac{(1-\varepsilon)L}{\theta_1}\sin\dfrac{\theta_1}{2}. \end{cases} \tag{13}$$

The torque balance eq. (3) should be rewritten as

$$\frac{W(T_2 - T_1)}{2}\left[H\cos\frac{\alpha}{2} + R_2\left(1 - \cos\frac{\theta_2}{2}\right) + R_1\left(1 - \cos\frac{\theta_1}{2}\right)\right] - M = 0. \tag{14}$$

Substituting eqs. (4), (5), and (9) into eq. (14), M can be expressed as

$$M = \frac{PWL^2}{2}\left[\left(\frac{1+\varepsilon}{\theta_2}\right)^2 - \left(\frac{1-\varepsilon}{\theta_1}\right)^2\right]. \tag{15}$$

Combining eqs. (13) and (15), there exists a mapping from α to M:

$$\alpha \xrightarrow{\text{Eq.(13)}} (\theta_1, \theta_2) \xrightarrow{\text{Eq.(15)}} M. \tag{16}$$

Therefore, the theoretical M-α curves can be obtained numerically based on eq. (16). For consistent comparison, the bending stiffness of the unit K is defined as the average slope of the M-α curve within the range $\alpha_0 \pm 10°$:

$$K = \frac{M(\alpha_0 + 10°) - M(\alpha_0 - 10°)}{20°}. \tag{17}$$

3.4 Kinematics of multiple units

To describe the shape morphing of the FCPA with multiple units, we employ a centerline-based kinematic model. As illustrated in Figure 3(c), each node along the centerline is characterized by a 2D pose (x_i, y_i, Φ_i), where (x_i, y_i) denotes the nodal position and Φ_i represents the tangent angle with respect to the X-axis.

For the i-th unit (with geometric parameters H, L, and ε_i), the center coordinates C_i can be derived from the preceding ($i-1$)-th node's pose:

$$\begin{bmatrix} x_{ci} \\ y_{ci} \end{bmatrix} = \mathbf{R}(\Phi_{i-1})\begin{bmatrix} 0 \\ -r_i \end{bmatrix} + \begin{bmatrix} x_{i-1} \\ y_{i-1} \end{bmatrix}, \tag{18}$$

where $r_i = \dfrac{S_i}{\alpha_{0i}}$ (α_{0i} and S_i are calculated based on eqs. (10)

−(12)). Here, $\mathbf{R}(\Phi_{i-1})$ is the rotation matrix defined as

$$\mathbf{R}(\Phi)=\begin{bmatrix}\cos\Phi & -\sin\Phi\\ \sin\Phi & \cos\Phi\end{bmatrix}. \tag{19}$$

The pose of the i-th node is then updated as

$$\begin{bmatrix}x_i\\ y_i\end{bmatrix}=\begin{bmatrix}x_{ci}\\ y_{ci}\end{bmatrix}-\mathbf{R}(\Phi_i)\begin{bmatrix}0\\ -r_i\end{bmatrix};\Phi_i=\Phi_{i-1}-\alpha_{0i}. \tag{20}$$

In the special case where $\alpha_{0i}=0$, the pose of the i-th node is directly given by

$$\begin{bmatrix}x_i\\ y_i\end{bmatrix}=\mathbf{R}(\Phi_{i-1})\begin{bmatrix}S_i\\ 0\end{bmatrix}+\begin{bmatrix}x_{i-1}\\ y_{i-1}\end{bmatrix};\Phi_i=\Phi_{i-1}. \tag{21}$$

Beginning from the 0-th node (x_0, y_0, Φ_0), the full centerline configuration (x_i, y_i, Φ_i) (for i = 1, 2, ..., n) can be determined through iterative computation. This kinematic model maps the geometric parameters H, L, and ε_i (i = 1, 2, ..., n) to the final configurations of FCPAs, thereby providing a platform for shape morphing design.

4 Experiments and results

4.1 Unit bending angle characterization

In this section, we investigate the influence of parameters on the unit bending angles α_0 (Figure 4(a)). According to eq. (10), α_0 only depends on the geometric parameters (ε and L/H). The numerical results of eq. (10) are shown in Figure 4(b), indicating that α_0 increases as ε and L/H increase. To validate the model, we design and characterize two groups of units: (1) units with varying ε (0–0.8) at a fixed L/H = 30 mm/25 mm, and (2) units with different L/H (0.83–1.5, maintaining $L + H$ = 55 mm) at a constant ε = 0.4. The experimental setup is shown in Figure 4(a). We first secure the lateral walls of the unit to two rigid fixtures and then pressurize the air chamber to 50 kPa. The bending angle is finally extracted through image processing. For each parameter set (ε, L/H), three specimens are tested and averaged to reduce random errors. Figure 4(c) and (d) presents the experimental results, which are in agreement with the theoretical predictions. The results also demonstrate that a single unit can achieve a bending deformation of up to 70°. Notably, within the typical fabrication ranges ($|\varepsilon| \leqslant 0.8$ and $0.8 \leqslant L/H \leqslant 1.6$), α_0 exhibits much higher sensitivity to ε than to L/H. These results provide insights for designing the local deformations of FCPAs.

4.2 Unit bending stiffness characterization

We next analyze the influence of parameters on the unit bending stiffness K, which is characterized by measuring the torque-angle relations. As shown in Figure 5(a), the experimental setup includes an electric rotary mobile platform (Y200RA100; Tai-Young Transmission Equipment Co., Ltd.), a torque sensor (TFF400; Futek), a smooth slide rail, a 2-axis mobile platform, and two fixtures. For a given unit, the experimental procedure consists of installation and measurement. Installation: secure the unit with the two fixtures, ensuring that its lateral walls remain straight; adjust the 2-axis mobile platform to align the unit coaxially with the torque sensor; move the electric rotary mobile platform to the force-free bending angle α_0 and reset the torque sensor. Measurement: pressurize the air chamber to a constant pressure; program the electric rotary mobile platform to rotate from α_0 to α_0 + 15° (or α_0 − 15°) at a speed of 0.25°/s; record the torque data at a sampling frequency of 50 Hz. Based on the measured torque-angle relations, K can be calculated based on eq. (17).

Our theoretical analysis indicates that K depends on the actuation pressure P and the geometric parameters ε, L, and H. We first characterize the bending stiffness of typical units (ε = 0, L = 30 mm, and H =25 mm) under different actuation pressures. Three specimens are tested. Figure 5(b) shows the measured torque-angle relations, which exhibit an approximately linear relationship between M and α. The corresponding bending stiffness, shown in Figure 5(c), increases

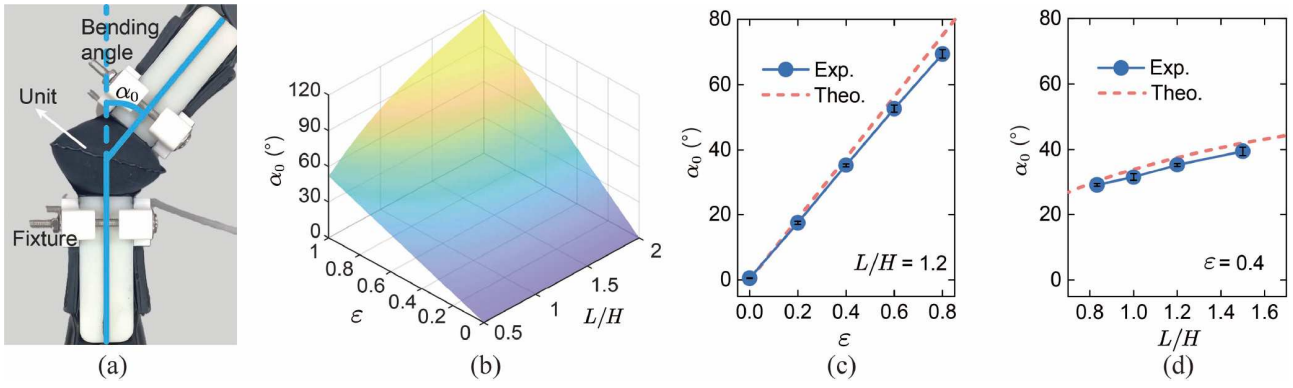

Figure 4 (Color online) Unit bending deformation. (a) Experimental setup for measuring the bending angles of the units; (b) the theoretical results of the bending angles varying with the asymmetry degree ε and the ratio L/H; (c) the relationship between the bending angles and ε; (d) the relationship between the bending angles and L/H. All the error bars in this work represent the standard deviations.

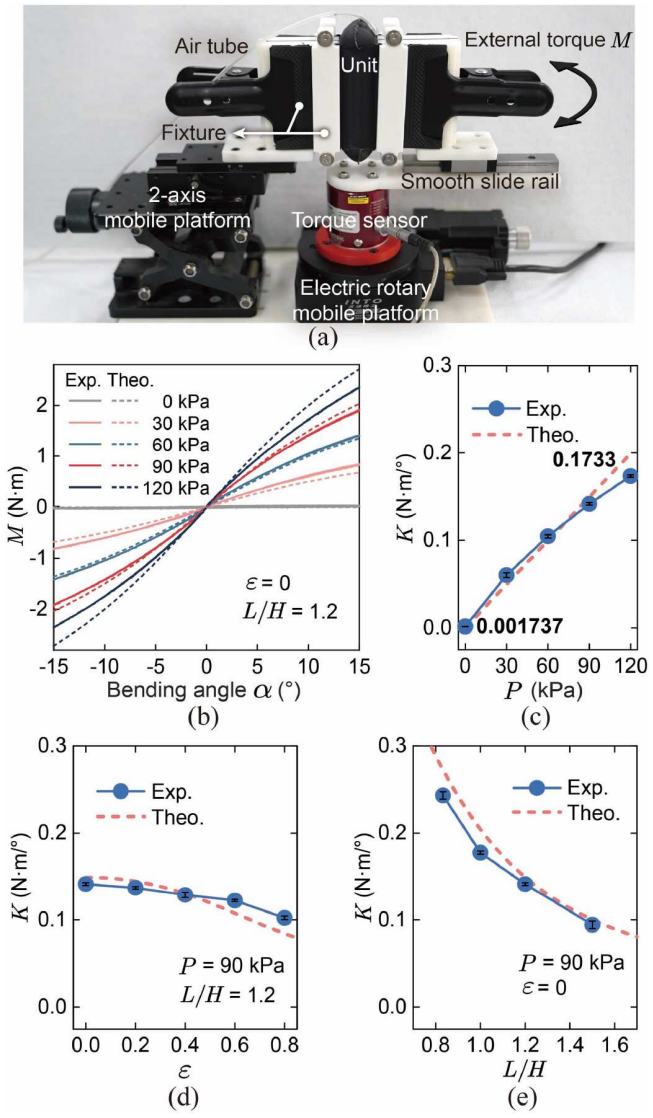

Figure 5 (Color online) Unit bending stiffness. (a) Experimental setup for measuring the torque-angle relations of the units. (b) Exemplary torque-angle relations of the units under different actuation pressures. The bending stiffness varies with (c) the actuation pressure P, (d) ε, and (e) L/H.

from 0.001737 to 0.1733 N m/° (99.8-fold) as the actuation pressure increases from 0 to 120 kPa. We then characterize the bending stiffness of two groups of units with varying ε or L/H at 90 kPa. For each parameter set (ε, L/H), three specimens are measured. The results, shown in Figure 5(d) and (e), indicate that K decreases as ε and L/H increase. Within the typical fabrication ranges ($|\varepsilon| \leqslant 0.8$ and $0.8 \leqslant L/H \leqslant 1.6$), K is strongly influenced by L/H but minimally sensitive to ε. These findings support the accuracy of our model and offer design guidelines for tuning the stiffness of FCPAs.

4.3 Performance of FCPAs

Among the geometric parameters, we conclude that the unit bending stiffness is primarily determined by L and H, while the unit bending angles are mainly controlled by ε. This enables an approximately decoupled design approach for FCPAs: (1) selecting appropriate L and H to meet application-specific stiffness and dimensional requirements, followed by (2) programming the asymmetry degree sequence ε_i (i = 1,2, ..., n) to achieve target morphing shapes. To facilitate the design, we develop a MATLAB-based visualization tool that displays the final FCPA configurations for any given input parameters (L, H, and ε_i (i = 1, 2, ..., n)). For example, our FCPA design tool successfully achieves target "S", "W", and "R" configurations (Figure 6(a) and Table 1), with the fabricated prototypes showing excellent shape fidelity (Figure 6(b) and Movie S1).

We also evaluate the stiffness variation capabilities of FCPAs. For the "1" shaped FCPA (Table 1), three-point bending tests (1 mm/s) are performed using a universal testing machine (68SC-2; Instron). Experimental results show that the compressive force increases from 0.19 to 81 N (at 30 mm displacement) as the actuation pressure rises from 0 to 120 kPa, corresponding to a 426-fold stiffness variation (Figure 6(c)). Similarly, for the "S" shaped FCPA, tensile tests (1 mm/s) reveal an increase from 0.10 to 46 N (at 40 mm displacement) under the same pressure range, equivalent to a 460-fold stiffness variation (Figure 6(d)). The FCPAs exhibit greater stiffness variation capabilities than single units. This difference arises because, in the unit bending stiffness characterization, the rigid fixtures restrict the deformation of lateral walls, which are free to deform in deflated FCPAs. These substantial stiffness variations allow the "1" shaped and the "S" shaped FCPAs to exhibit the softness of fabric when deflated, yet become rigid enough to bear or lift a load of over 5 kg when inflated (Figure 6(e) and (f) and Movie S1). The results collectively demonstrate the excellent performance of FCPAs in shape morphing, stiffness variation, and load capacity.

4.4 Applications in soft wearable robots

To demonstrate the potential of FCPAs in soft wearable applications, we preliminarily developed a soft exosuit for shoulder abduction assistance. Given the high torque requirements of shoulder abduction, we set the FCPA parameters L and H to 25 and 30 mm, respectively (L/H = 0.83), to enhance the structural stiffness in the activated state. To match the profile beneath the human shoulder, the FCPA adopts a three-segment configuration, where the two outer segments straighten to conform to the torso and arm, while the central segment bends to accommodate the axilla (Figure 7(a) and Table 1). This anatomical compatibility helps distribute interaction forces between the exosuit and the body, thus improving wearing comfort. Additionally, the maximum abduction angle is adjustable; here, it is set to 112° to cover

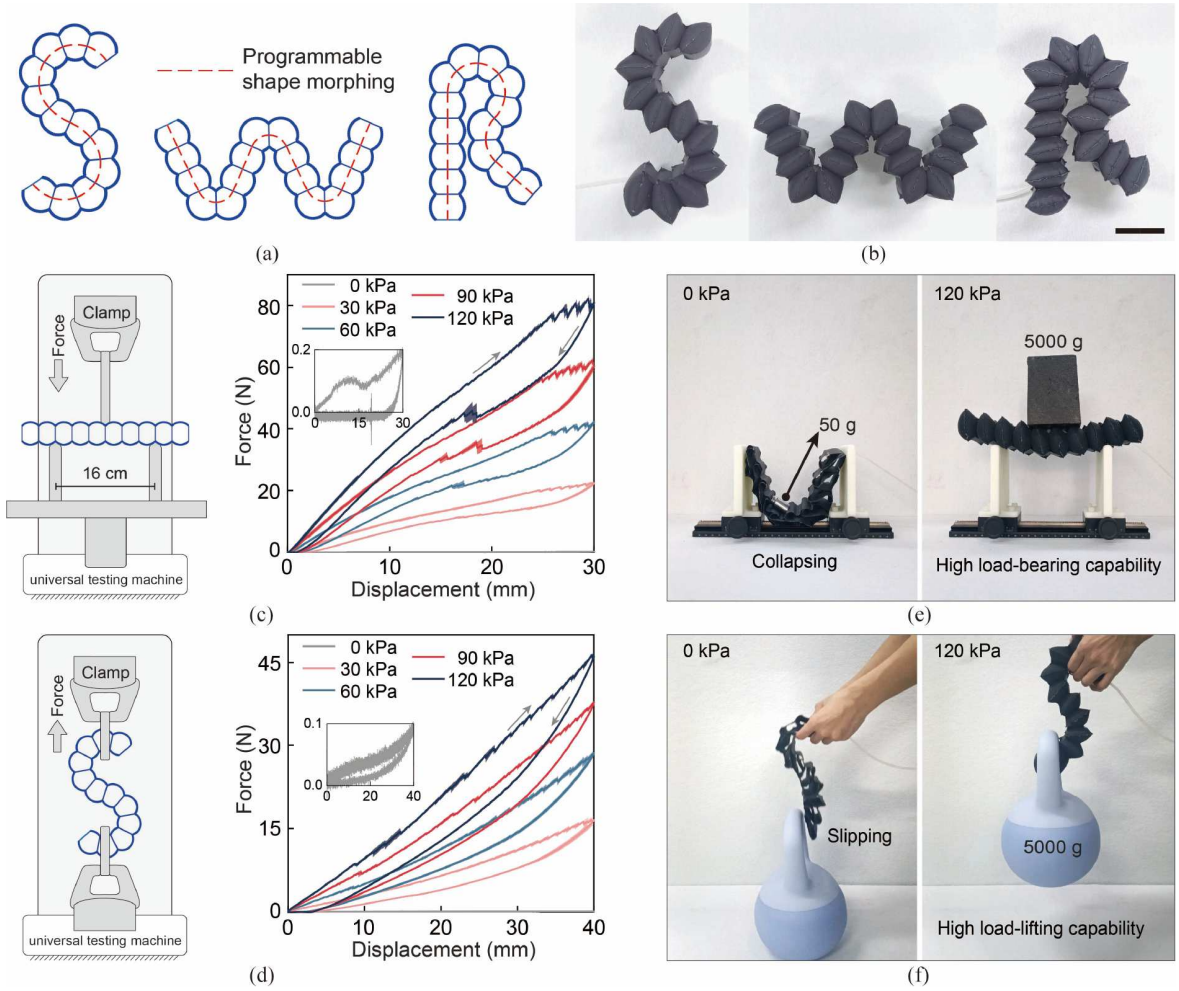

Figure 6 (Color online) FCPAs with programmable shape morphing and high stiffness variation. (a) Programming the shape morphing of FCPAs based on the kinematics of multiple units; (b) the fabricated FCPAs match the target shapes. Scale bar, 5 cm. (c) Experimental setup and results of the three-point bending tests of the "1" shaped FCPA. (d) Experimental setup and results of the tensile tests of the "S" shaped FCPA. (e) Load-bearing capabilities of the "1" shaped FCPA. (f) Load-lifting capabilities of the "S" shaped FCPA.

Table 1 Design parameters of the FCPAs in this work

Prototype	L (mm)	H (mm)	ε_i (i = 1, 2, ..., n)
"S" shaped	30	25	0.4; 0.4; 0.4; 0.4; 0.25; −0.25; −0.4; −0.4; −0.4; −0.4
"W" shaped	30	25	0; 0; 0; 0.7; 0.7; 0; 0; −0.7; −0.7; 0; 0; 0.7; 0.7; 0; 0; 0
"R" shaped	30	25	0; 0; 0; 0; 0; 0.5; 0.5; 0,5; 0.5; 0.4; −0.5; −0.5; 0; 0
"1" shaped	30	25	0; 0; 0; 0; 0; 0; 0; 0; 0; 0
Shoulder exosuit	25	30	0; 0; 0; 0; 0; 0.3; 0.3; 0.3; 0; 0; 0; 0

the most frequent range of arm movement. For force transmission, the FCPA is integrated into the exosuit by sewing and buttoning it to a waistcoat and an arm strap (Figure 7(b)).

We first verify the soft exosuit on a mannequin with a smooth spherical shoulder joint. Upon inflation, the FCPA morphs into the target shape, abducting the mannequin's arm from its resting position (Figure 7(c) and Movie S2). Two markers attached to the arm are tracked by a camera system (Optitrack, Prime 13) to measure abduction angles. Under 120 kPa, the measured abduction angles reach 84°, 76°, and 69° when the mannequin holds additional loads of 0, 250, and 500 g (Figure 7(d)), corresponding to assistive torques of approximately 1.9, 3.3, and 4.5 N m. We also test the wearability of the soft exosuit on a healthy subject. The subject can complete the donning process alone within 80 s, move freely when unassisted, and passively abduct the arm beyond 75° with assistance (Movie S2). These results validate the effectiveness of our FCPAs in developing SWRs.

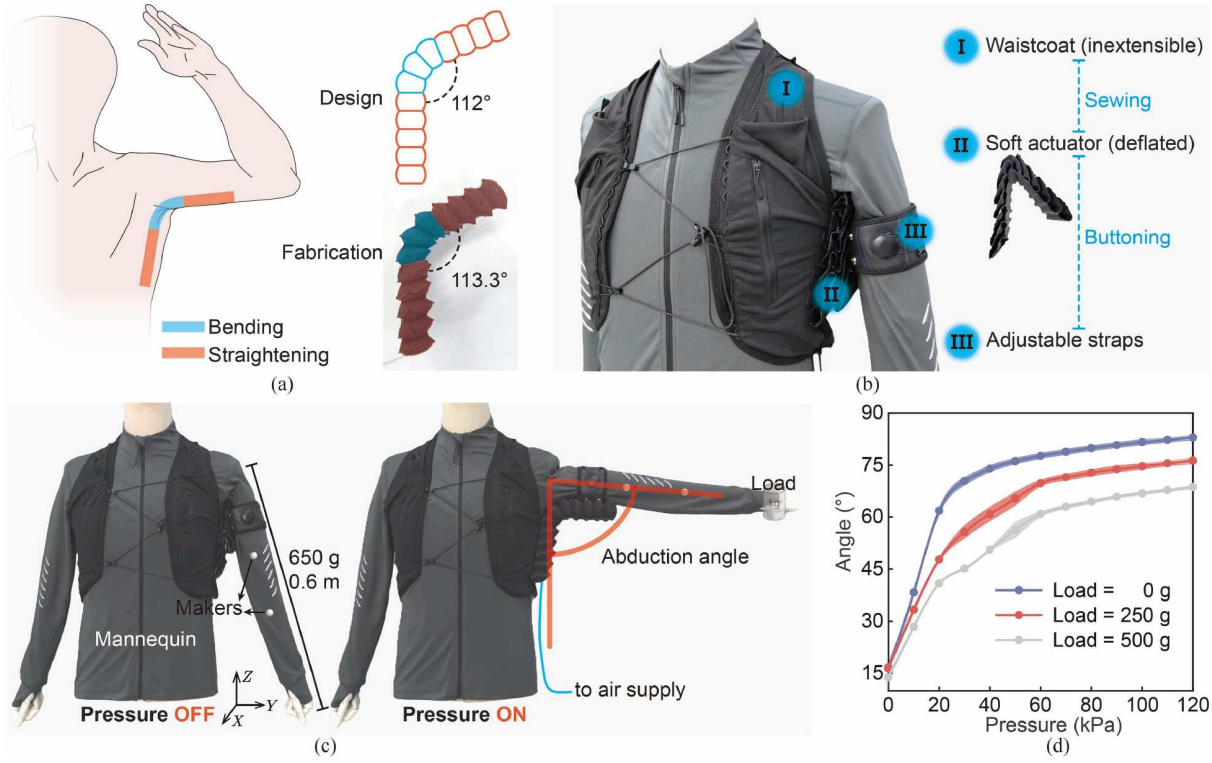

Figure 7 (Color online) A soft exosuit for shoulder abduction assistance based on the FCPAs. (a) Customizing the FCPA based on the profile beneath the human shoulder; (b) components of the soft exosuit; (c) verification on a mannequin. The soft exosuit assists in abducting the arm from its resting position. (d) Characterization results of the shoulder abduction angle under varying actuation pressures and loads.

Table 2 Comparison of the FCPAs and other stiffness-tunable shape-morphing mechanisms

Reference	Stiffness variation capabilities (-fold)	Actuation	Fully flexible materials?
[28]	130	Thermal-driven	No
[31]	N/A	Positive pressure	No
[33]	~2	Positive pressure	Yes
[34]	53	Negative pressure	No
[36]	>350	Cable-driven	No
This work	>420	Positive pressure	Yes

5 Conclusion

In this work, by mimicking the structural features of bulliform cells, we propose a class of fabric-based cellular pneumatic actuators (FCPAs) that can achieve simultaneous shape morphing and stiffness variation. The activated configuration of the FCPAs is solely determined by their geometric parameters, and their structural stiffness is widely tunable by adjusting the actuation pressure. To facilitate the FCPA design, we establish a theoretical model that predicts local deformation and stiffness, as well as global kinematics. Experimental results validate the model's accuracy and demonstrate the excellent performance of the FCPAs in shape morphing, stiffness variation, and load capacity. Unlike most existing stiffness-tunable shape-morphing mechanisms, the FCPAs are entirely composed of flexible materials while achieving a remarkable stiffness variation of over 420-fold (Table 2). These advantages make FCPAs highly promising for effective and comfortable soft wearable robots, such as the soft shoulder exosuit demonstrated in this work. However, we should mention that the current FCPA designs are limited to 2D deformations. While the developed soft exosuit leverages compliant pneumatic actuation for ease of implementation, it relies on bulky pneumatic control systems. Future work will focus on extending FCPA designs to enable 3D deformations, integrating portable and noiseless pneumatic control systems, and systematically advancing FCPA-based soft wearable assistive robots for real-world applications.

Acknowledgements This work was supported by the National Key R&D Program of China (Grant No. 2024YFB4707504), the National Natural Science Foundation of China (Grant No. 52025057), the Science and

Technology Commission of Shanghai Municipality (Grant No. 24511103400), and the Xplorer Prize.

Supporting Information The supporting information is available online at tech.scichina.com and link.springer.com. The supporting materials are published as submitted, without typesetting or editing. The responsibility for scientific accuracy and content remains entirely with the authors.

References

1 Zhou Y M, Hohimer C J, Young H T, et al. A portable inflatable soft wearable robot to assist the shoulder during industrial work. Sci Robot, 2024, 9: eadi2377
2 Hong T, Lee C, Chang S, et al. Design of a fully-soft lift-assist wearable suit powered by flat inflatable artificial muscles. IEEE Robot Autom Lett, 2025, 10: 4428–4435
3 Proietti T, O'Neill C, Gerez L, et al. Restoring arm function with a soft robotic wearable for individuals with amyotrophic lateral sclerosis. Sci Transl Med, 2023, 15: eadd1504
4 Feng M, Yang D, Sun J, et al. A pilot study on fabric-based pneumatic soft gloves for assisting patients with severe brachial plexus injury. IEEE Trans Biomed Eng, 2025, 72: 3174–3185
5 Huang W C, Feng M, Yang D Z, et al. Low-resistance, high-force, and large-ROM fabric-based soft elbow exosuits with adaptive mechanism and composite bellows. Sci China Tech Sci, 2023, 66: 24–32
6 Xiloyannis M, Alicea R, Georgarakis A M, et al. Soft robotic suits: State of the art, core technologies, and open challenges. IEEE Trans Robot, 2022, 38: 1343–1362
7 Sharma B, Phan P T, Davies J, et al. Soft upper-limb wearable robotic devices: Technology and applications. Adv Intell Syst, 2024, 6: 2400266
8 Pan M, Yuan C, Liang X, et al. Soft actuators and robotic devices for rehabilitation and assistance. Adv Intell Syst, 2021, 4: 2100140
9 Xu S, Hu X, Yang R, et al. Transforming machines capable of continuous 3D shape morphing and locking. Nat Mach Intell, 2025, 7: 703–715
10 Tang J, Chen Z, Cai Y, et al. Stretch-activated reprogrammable shape-morphing composite elastomers. Adv Funct Mater, 2022, 32: 2203308
11 Luo Y, Patel D K, Li Z, et al. Intrinsically multistable soft actuator driven by mixed-mode snap-through instabilities. Adv Sci, 2024, 11: 2307391
12 Connolly F, Walsh C J, Bertoldi K. Automatic design of fiber-reinforced soft actuators for trajectory matching. Proc Natl Acad Sci USA, 2016, 114: 51–56
13 Baines R, Patiballa S K, Gorissen B, et al. Programming 3D curves with discretely constrained cylindrical inflatables. Adv Mater, 2023, 35: 2300535
14 Guo X, Li W, Fang F, et al. Encoded sewing soft textile robots. Sci Adv, 2024, 10: eadk3855
15 Huang K, Yuan R, Song Z, et al. Differentiable ANCF-based kinematic modeling of soft pneumatic robots for design optimization. IEEE ASME Trans Mechatron, 2025, 30: 2826–2834
16 Jiang C, Wang D, Zhao B, et al. Modeling and inverse design of bio-inspired multi-segment pneu-net soft manipulators for 3D trajectory motion. Appl Phys Rev, 2021, 8: 041416
17 Jones T J, Jambon-Puillet E, Marthelot J, et al. Bubble casting soft robotics. Nature, 2021, 599: 229–233
18 Becker K, Teeple C, Charles N, et al. Active entanglement enables stochastic, topological grasping. Proc Natl Acad Sci USA, 2022, 119: e2209819119
19 Narang Y S, Aktaş B, Ornellas S, et al. Lightweight highly tunable jamming-based composites. Soft Robotics, 2020, 7: 724–735
20 Zhou J, Chen Y, Hu Y, et al. Adaptive variable stiffness particle phalange for robust and durable robotic grasping. Soft Robotics, 2020, 7: 743–757
21 Zuo S, Li H, Hua Z, et al. A novel jamming structure with interlocking mechanism towards applications in wearable robots. IEEE Robot Autom Lett, 2022, 7: 6305–6312
22 Guo X Y, Li W B, Gao Q H, et al. Self-locking mechanism for variable stiffness rigid-soft gripper. Smart Mater Struct, 2020, 29: 035033
23 Althoefer K. Antagonistic actuation and stiffness control in soft inflatable robots. Nat Rev Mater, 2018, 3: 76–77
24 Bruder D, Graule M A, Teeple C B, et al. Increasing the payload capacity of soft robot arms by localized stiffening. Sci Robot, 2023, 8: eadf9001
25 Hwang D, Barron Iii E J, Haque A B M T, et al. Shape morphing mechanical metamaterials through reversible plasticity. Sci Robot, 2022, 7: eabg2171
26 Zhang Y ‐F, Zhang N, Hingorani H, et al. Fast-response, stiffness-tunable soft actuator by hybrid multimaterial 3D printing. Adv Funct Mater, 2019, 29: 1806698
27 Gao T, Siéfert E, DeSimone A, et al. Shape programming by modulating actuation over hierarchical length scales. Adv Mater, 2020, 32: 2004515
28 Gao T, Bico J, Roman B. Pneumatic cells toward absolute Gaussian morphing. Science, 2023, 381: 862–867
29 Oh N, Rodrigue H. Toward the development of large-scale inflatable robotic arms using hot air welding. Soft Robotics, 2023, 10: 88–96
30 Wu C, Liu H, Lin S, et al. Shape morphing of soft robotics by pneumatic torsion strip braiding. Nat Commun, 2025, 16: 3787
31 Wu J, Wu M, Chen W, et al. Multimodal soft amphibious robots using simple plastic-sheet-reinforced thin pneumatic actuators. IEEE Trans Robot, 2024, 40: 1874–1889
32 Zhang Z, Long Y, Chen G, et al. Soft and lightweight fabric enables powerful and high-range pneumatic actuation. Sci Adv, 2023, 9: eadg1203
33 Feng M, Yang D, Ren L, et al. X-crossing pneumatic artificial muscles. Sci Adv, 2023, 9: eadi7133
34 Yang D, Feng M, Gu G. High-stroke, high-output-force, fabric-lattice artificial muscles for soft robots. Adv Mater, 2024, 36: 2306928
35 Chen T, Yang X, Zhang B, et al. Scale-inspired programmable robotic structures with concurrent shape morphing and stiffness variation. Sci Robot, 2024, 9: eadl0307
36 Yang X, Wang Z, Zhang B, et al. Self-sensing robotic structures from architectured particle assemblies. Adv Intell Syst, 2022, 5: 2200250
37 Yang X, Chen Y, Chen T, et al. Active fabrics with controllable stiffness for robotic assistive interfaces. Adv Mater, 2024, 36: 2404502
38 Matschi S, Vasquez M F, Bourgault R, et al. Structure-function analysis of the maize bulliform cell cuticle and its potential role in dehydration and leaf rolling. Plant Direct, 2020, 4: e00282
39 Chandler T G J, Ferria J, Shorthose O, et al. Mechanics of pressurized cellular sheets. J R Soc Interface, 2025, 22: 2024065